Order-to-disorder transition in the XY-like quantum magnet Cs$_2$CoCl$_4$ induced by noncommuting applied fields

M. Kenzelmann,[1] R. Coldea,[1,2,3] D. A. Tennant,[1,3] D. Visser,[4,5,6] M. Hofmann,[7] P. Smeibidl,[7] and Z. Tylczynski[8]

[1]*Oxford Physics, Clarendon Laboratory, Oxford OX1 3PU, United Kingdom*
[2]*Oak Ridge National Laboratory, Oak Ridge, Tennessee 37831*
[3]*ISIS Facility, Rutherford Appleton Laboratory, Oxon OX11 0QX, United Kingdom*
[4]*NWO-EW, ISIS Facilty, Rutherford Appleton Laboratory, Chilton, Didcot OX11 0QX, United Kingdom*
[5]*Department of Physics, University of Warwick, Gibbet Hill Road, Coventry CV4 7AL, United Kingdom*
[6]*IRI, Technical University Delft, Mekelweg 15, 2629JB Delft, The Netherlands*
[7]*Hahn-Meitner-Institut, BENSC, 14109 Berlin, Germany*
[8]*Institute of Physics, Adam Mickiewicz University, Umultowska 85, 61-614 Poznan, Poland*

We explore the effects of noncommuting applied fields on the ground-state ordering of the quasi-one-dimensional spin-$\frac{1}{2}$ XY-like antiferromagnet Cs$_2$CoCl$_4$ using single-crystal neutron diffraction. In zero-field, interchain couplings cause long-range order below $T_N = 217(5)$ mK with chains ordered antiferromagnetically along their length and moments confined to the (b,c) plane. Magnetic fields applied at an angle to the XY planes are found to initially stabilize the order by promoting a spin-flop phase with an increased perpendicular antiferromagnetic moment. In higher fields the antiferromagnetic order becomes unstable and a transition occurs to a phase with no long-range order in the (b,c) plane, proposed to be a spin-liquid phase that arises when the quantum fluctuations induced by the noncommuting field become strong enough to overcome ordering tendencies. Magnetization measurements confirm that saturation occurs at much higher fields and that the proposed spin-liquid state exists in the region $2.10 < H_{SL} < 2.52$ T $\| a$. The observed phase diagram is discussed in terms of known results on XY-like chains in coexisting longitudinal and transverse fields.

I. INTRODUCTION

A promising area for the study of zero-temperature quantum phase transitions is that of quantum spin systems in noncommuting applied magnetic fields.[1] Such noncommuting terms introduce quantum fluctuations into the $T=0$ ground state which, for large enough fields, can completely disorder the system. Such a situation has been studied in considerable detail in the three-dimensional Ising ferromagnet LiHoF$_4$ in a transverse magnetic field.[2] However, due to its high dimensionality, the system behaves in a mean-field-like way. In this paper we consider a one-dimensional (1D) quantum magnet and the effects of a noncommuting field on its ground state.

The scenario that we investigate experimentally is that of the 1D spin-$\frac{1}{2}$ XXZ model [$\mathcal{H}_{XXZ}(\Delta)$] in a noncommuting field ($\mathcal{H}_{APP}$), given by the Hamiltonian

$$\mathcal{H} = \mathcal{H}_{XXZ}(\Delta) + \mathcal{H}_{APP}, \qquad (1)$$

where

$$\mathcal{H}_{XXZ}(\Delta) = J \sum_i \left(S_i^x S_{i+1}^x + S_i^y S_{i+1}^y + \Delta S_i^z S_{i+1}^z \right), \qquad (2)$$

$$\mathcal{H}_{APP} = \sum_i B^x S_i^x + B^z S_i^z, \qquad (3)$$

$J > 0$ is the antiferromagnetic (AF) exchange constant, and $\Delta < 1$ is the anisotropy parameter (a $g_{x,z} \mu_B$ factor is incorporated in the magnetic field $B^{x,z}$). The operators S^α, where $\alpha = x, y, z$, are the usual spin operators for spin $\frac{1}{2}$, and the applied field term does not commute with the exchange Hamiltonian $[\mathcal{H}_{XXZ}(\Delta), \mathcal{H}_{APP}] \neq 0$ for $|\Delta| \neq 1$ and $B^x \neq 0$. Indeed, the system we shall study, Cs$_2$CoCl$_4$, is an excellent realization of $\mathcal{H}_{XXZ}(\Delta)$, where $\Delta = 0.25$, and therefore should be well approximated by the famous XY model ($\Delta = 0$).[3]

The physics of the $\mathcal{H}_{XXZ}(\Delta)$ model at $\Delta = 0$ is well known in the absence of a magnetic field, i.e., $B^x = B^z = 0$. It is that of a 1D noninteracting Fermi gas as shown by the Jordan-Wigner transformation.[4] The effect of a field along z, $B^z \neq 0$ (commuting), is trivial; it acts as a chemical potential and changes the filling level of the fermions in the chain, inducing magnetization along z. Below a critical field, B_C^z, representing the field of complete saturation of the chain, the excitation spectrum remains gapless and the $T=0$ correlation functions fall algebraically as power laws. In contrast, the physics for the case of a field along x, $B^x \neq 0, B^z = 0$, is neither trivial nor widely known.

The action of noncommuting field B^x on $\mathcal{H}_{XXZ}(0)$ has been considered theoretically by Kurmann *et al.*[5,6] From these studies it was found that the in-plane field has two effects: (i) it breaks the U(1) symmetry of the XY model to a lower, Ising-like, symmetry which brings the ground state to long-range order (LRO) at $T=0$ into a spin-flop-type Néel state. In fact at a special coupling, $B^x = \sqrt{2}J$, the spin-flop Néel state is the exact $T=0$ ground state. (ii) The second effect is to introduce quantum fluctuations into the system. At high fields this causes a phase transition to occur where the fluctuations become large enough to destroy the LRO
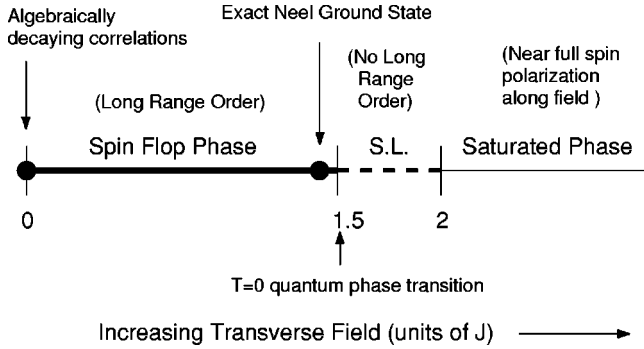
65 144432-1

FIG. 1. Schematic representation of the phases of the ground state of the *XY* model as a function of applied transverse field as proposed by Kurmann *et al.* (Refs. 5 and 6) (see text for details). In the absence of a field the correlation functions decay as a power law. Small magnetic fields induce perpendicular long-range-ordered antiferromagnetism and the ordering is characterized as a spin-flop phase. At a field $\sqrt{2}J$ the classical Néel state is the exact $T=0$ ground state. The antiferromagnetism is rapidly suppressed at higher fields by the quantum fluctuations induced by the noncommuting field. Above about $1.5J$ long-range order is destroyed by these fluctuations and the ground state is characterized as a spin-liquid (SL) state with exponentially decaying correlations in the spin components perpendicular to the field. Above a crossover field of about $2J$ nearly all the spin moments are aligned along the field direction and the physics here is characterized as a saturated phase.

altogether. This disordering field is below that where the system reaches its saturation point. This phase transition is therefore a nontrivial quantum phase transition through a quantum critical point with the noncommuting field as a control parameter. Figure 1 shows a schematic outline of the physics of the *XY* model in a transverse field.

The theoretical studies[5,6] suggest that this behavior is generic to a wide class of magnets in noncommuting fields, and a disordered spin-liquid (SL) phase is expected for all $H_{XXZ}(|\Delta| \neq 1)$ in Eq. (1). Spin-liquid phases such as this are generally gapped (evidenced by the exponentially decaying correlations in the zero-temperature ground state) and therefore robust against small perturbations. We therefore expect the effects of nonzero Δ and interchain coupling to modify the transition fields in Fig. 1 but not to change their qualitative content.

In this paper we present a detailed study of the ground-state ordering of the quasi-1D *XY*-like antiferromagnet Cs_2CoCl_4 in noncommuting fields from zero to well above saturation. The crystalline and magnetic properties of Cs_2CoCl_4 and the experimental tool of neutron diffraction will be introduced in Sec. II.

Section III presents the observed commensurate magnetic structure and its field dependence. The structure is that of magnetic chains which are ordered antiferromagnetically along their lengths with ordered moments lying in the (b,c) plane. The experimental results show that an applied field initially further stabilizes the ordered structure (spin-flop phase), but as the field increases, fluctuations induced by field noncommutation cause a sharp transition to a new phase which we propose to be the spin-liquid phase discussed above. Study of the ferromagnetic component (Sec. III D)

confirms that the saturation field is higher still, and that the proposed spin-liquid phase exists in the region $2.10 < H_{SL} < 2.52$ T$\|a$.

An extended discussion of our results is given in Sec. IV. The observation of commensurate order $[\mathbf{k}=(0,\frac{1}{2},\frac{1}{2})]$ in Cs_2CoCl_4 is related to the effective Ising-type interchain coupling (Sec. IV A) and compared with the quasielastic results of Yoshizawa *et al.*[7] A microscopic study of the ordering is presented in Sec. IV B based on a mean-field analysis of the ground-state energy. The magnitude of the ordered moment is established in Sec. IV C. Finally, in Sec. IV D the magnetization curve is critically examined and compared with known results for anisotropic spin chains in noncommuting applied fields.

II. EXPERIMENTAL DETAILS

A. Properties of Cs_2CoCl_4

Cs_2CoCl_4 has been proposed as a spin-$\frac{1}{2}$ quasi-1D *XY*-like antiferromagnet with chains running along the *b* direction. Heat-capacity measurements[8] showed a broad maximum (characteristic of low-dimensional systems) around $T \simeq 0.9$ K and the overall temperature dependence agreed well with numerical predictions[9] for a $S=\frac{1}{2}$ *XY*-like AF chain with exchange coupling $J=0.23(1)$ meV. A small lambda-type anomaly observed in the specific heat at $T_N=222$ mK was interpreted[8] as indicating a phase transition to a magnetically ordered phase caused by small couplings between chains. The in-plane magnetic susceptibility[10,11] also indicated magnetic ordering below 222 mK and the temperature dependence between 40 mK and 4.2 K was in excellent agreement with numerical calculations for AF *XXZ* chains with $\Delta=0.25$ in Eq. (2).

Quasielastic neutron-scattering experiments[7] showed that between $T=0.3$ and 0.6 K the critical scattering of Cs_2CoCl_4 is sheetlike perpendicular to the *b* axis, thus confirming the proposed quasi-1D character of the magnetic properties. Interestingly, the critical scattering is driven partly to incommensurate positions due to competing interchain interactions. Those earlier diffraction experiments[7] concentrated on the critical scattering at temperatures above the ordering transition of 0.22 K inferred by macroscopic measurements. As the ordering in this material promises to have some unusual and challenging features, we undertook detailed neutron-diffraction experiments to determine the magnetic structure and the behavior in applied noncommuting magnetic fields at temperatures much below the proposed ordering transition of 0.22 K.

Cs_2CoCl_4 crystallizes in the orthorhombic (and nonsymmorphic) space group *Pnma* (D_{2h}^{16}, No. 62).[12] The crystal structure is shown schematically in Fig. 2. The lattice parameters at 0.3 K are[13,7] $a=9.71$ Å, $b=7.27$ Å, and $c=12.73$ Å. The magnetic ions, Co^{2+} with spin $\tilde{S}=\frac{3}{2}$, occupy site 4*c* in the unit cell at positions[13,14]

    1.   (0.235,0.25,0.422),

    2.   (0.735,0.25,0.078),
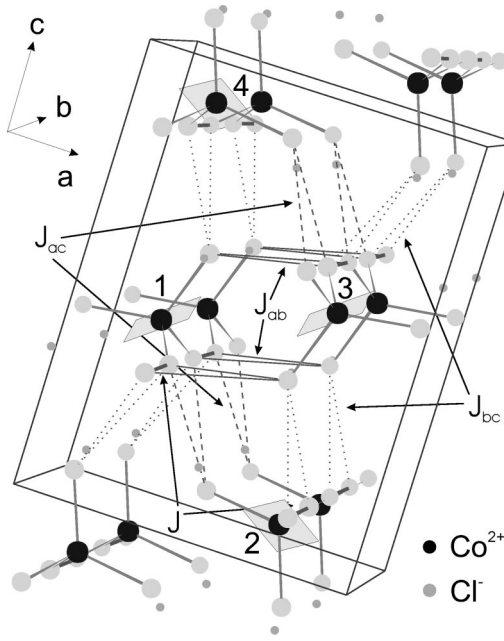
FIG. 2. Crystal structure of Cs_2CoCl_4. The figure shows 12 Co^{2+} ions, each surrounded by a distorted tetrahedron of Cl^- ions. The Co^{2+} ions interact mainly via an AF superexchange interaction J along the b axis, forming AF spin chains which interact weakly via superexchange interactions J_{ab}, J_{ac}, and J_{bc} as explained in the text. The shaded rectangular planes indicate possible orientations of the XY easy planes following Ref. 15.

3. $(0.765, 0.75, 0.578)$,

4. $(0.265, 0.75, 0.922)$.

Neighboring spins interact via a superexchange interaction involving a bridge of two Cl^- ions with the path Co^{2+}-Cl^--Cl^--Co^{2+}. The shortest Cl^--Cl^- distance is between neighbors along the b axis separated by 3.63 Å . As this is close to twice the ionic radius of Cl a sizeable overlap of electron wave functions contributing to the exchange integral is expected.

Among other possible exchange paths are J_{ac} between sites 1 and 2 ($d_{Cl^--Cl^-} = 4.05$ Å), J_{ab} between sites 1 and 3 ($d_{Cl^--Cl^-} = 4.04$ Å), and J_{bc} between sites 1 and 4 ($d_{Cl^--Cl^-} = 4.01$ Å). Since the overlap of the electronic wave functions decreases very rapidly (approximately exponentially) with distance, these exchange paths are expected to yield much smaller interactions than the coupling J along b such that Cs_2CoCl_4 can be regarded as a system of weakly coupled spin chains along the b axis.

Each Co^{2+} ion is tetrahedrally coordinated by Cl^- ligands. Small distortions from a perfect tetrahedron lead to a splitting of the $\tilde{S} = \frac{3}{2}$ orbital singlet state into two Kramers doublets with a separation $2D = 1.3(1)$ meV. The magnetic exchange energy is much lower than the interdoublet separation and therefore only the lowest-lying doublet states participate in the low-energy dynamics at low temperatures ($T \ll D$). Projecting the Heisenberg exchange between the true

spins onto the lowest-lying doublet of $|\pm \frac{1}{2}\rangle$ states gives an effective spin-$\frac{1}{2}$ Hamiltonian with XY-like exchange, $\mathcal{H}_{XXZ}$ in Eq. (2) with $\Delta = 0.25$.

Rotations of the $CoCl_4$ tetrahedra in the unit cell lead to different orientations of the XY easy plane between sites (1,3) and (2,4) and give the b axis as the only common in-plane direction for all sites. The main distortion of the $CoCl_4$ unit from a perfect tetrahedron is due to one of the four Cl^- ions being rotated by several degrees around the b axis with respect to the central Co^{2+} ion and previous studies[15] proposed that the normal to the XY easy plane (z axis) bisects this large angle. This gives the z-axis direction $(\sin \beta, 0, \cos \beta)$ on sites (1,3) and $(-\sin \beta, 0, \cos \beta)$ on sites (2,4) with $\beta = -38.8°$. The shaded rectangular planes in Fig. 2 show the XY planes in this case. Another possibility is that the z axis is along the vector connecting the central Co^{2+} ion with the Cl^- ion rotated most, and in that case $\beta = +19.4°$.

B. Experimental method

A high-quality 6.45 g single crystal of Cs_2CoCl_4 was grown from solution. The crystal was aligned with its $(0,k,l)$ plane in the horizontal scattering plane and was cooled to temperatures between $T = 80$ and 250 mK using an Oxford Instruments dilution refrigerator insert placed inside a vertical 7 T superconducting magnet.

Neutron-diffraction measurements were made at the Hahn-Meitner Institut in Berlin, Germany. The two-axis crystal diffractometer E6 was employed with an incident energy of $E_i = 14.72$ meV and with a pyrolytic graphite (PG) monochromator in double-focusing mode to increase the neutron flux at the sample position. The scattered neutrons were counted in a 20° wide BF_3 detector bank with position sensitivity along the horizontal direction giving 200 channels. This gave an angular resolution of 0.1° in the total scattering angle 2Θ. The intensities of nuclear and magnetic Bragg reflections were measured as a function of both 2Θ and the sample rotation angle Ψ, thus constructing full two-dimensional (2D) maps of the scattering intensity in the $(\Psi, 2\Theta)$ plane. This allowed simultaneous coverage of both magnetic signal and background. Typical counting times were 5 min per 2D map to determine the total integrated intensity, and 40 s for a 2Θ scan at the peak center to extract the peak intensity. A two-dimensional Gaussian with adjustable rotation of the main axes of the ellipsoid gave a good account of the observed peak line shapes in both Ψ and 2Θ, and the intensities of the Bragg reflections were obtained from least-square fits to the experimental data to reduce the sum of discrepancies χ^2.

III. EXPERIMENTAL RESULTS

A. Magnetic order in zero field

Upon cooling below $T_N = 217$ mK extra Bragg reflections were observed at the commensurate $(0, n+0.5, m+0.5)$ reciprocal-lattice positions with n and m integers, indicating a transition to a magnetically long-range-ordered state. Figure 3 shows the temperature dependence of the $(0, 0.5, -1.5)$ AF reflection showing the onset of order below
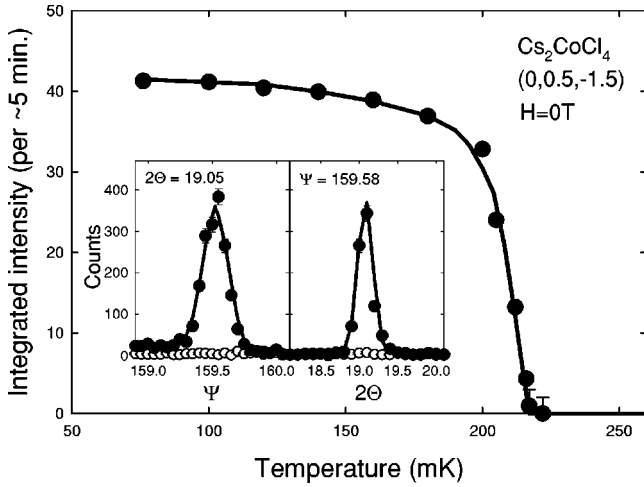
FIG. 3. Integrated intensity of the antiferromagnetic $(0,0.5,-1.5)$ reflection vs temperature in zero external field. Intensity units are the same as in Table I. The solid line is a guide to the eye. The inset shows the Bragg-peak intensity as a function of Ψ (left) and 2Θ (right) at temperatures below (solid circles) and above (open circles) the transition temperature $T_N = 217$ mK. Solid lines come from a two-dimensional fit to the data in the $(\Psi, 2\Theta)$ plane as described in the text.

T_N. The extracted transition temperature $T_N = 217$ mK is consistent with that inferred from specific-heat and susceptibility measurements.[8,11]

The observed magnetic reflections are associated with a magnetic ordering wave vector $\mathbf{k} = (0, \frac{1}{2}, \frac{1}{2})$. To determine the magnetic structure we first used group theory to identify the spin configurations consistent with the wave vector $\mathbf{k}$ for the given crystal symmetry, and second, we compared the structure factor of possible spin configurations with the experimentally observed magnetic Bragg-peak intensities.

The group-theory analysis and determination of the symmetry-allowed basis vectors are presented in the Appendix. After comparison of the data with the possible eigenvectors, we find that the observed structure belongs to the Γ^{10} irreducible representation with eigenvector ϕ^{10} given in Eq. (A5). This eigenvector has six degrees of freedom corresponding to the three components of the moments $\mathbf{m}_1$ and $\mathbf{m}_3$. Using spherical coordinates these can be written as $\mathbf{m}_1 = M_1(\sin\vartheta_1, \cos\vartheta_1\cos\phi_1, \cos\vartheta_1\sin\phi_1)$ and $\mathbf{m}_3 = M_3(\sin\vartheta_3, \cos\vartheta_3\cos\phi_3, \cos\vartheta_3\sin\phi_3)$. For $\vartheta_{1,3} = 0$, spins are in the (b,c) plane and ϕ is the azimuthal angle with the b axis.

Figure 4(a) shows a pictorial representation of the ϕ^{10} eigenvector in Eq. (A5) in the special case of ordered spins contained in the (b,c) plane, making a small angle with the b axis ($\phi_1 = -\phi_3$) and having equal magnitude on all sites ($|\mathbf{m}_1| = |\mathbf{m}_3|$). The structure can be described in terms of antiferromagnetic chains along b with a certain ordering pattern between adjacent chains. Starting with the basic structure shown in Fig. 4(a) other distinct domains shown in Figs. 4(b)–4(d) can be constructed by changing the sign of either the b- or the c-spin components, or the relative phase between chains 1 and 3 (for details see the Appendix).
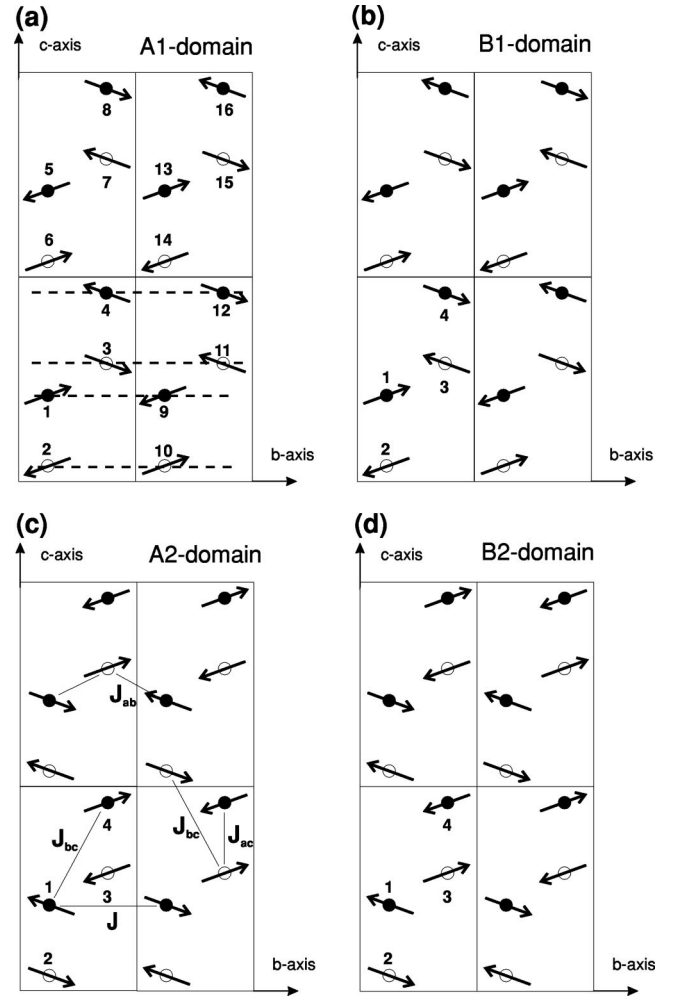

FIG. 4. Magnetic structure of Cs_2CoCl_4. Spins (indicated by arrows) order antiferromagnetically along chains [shown by dashed lines in (a)]. Ordered moments are contained in the (b,c) plane and make a small angle with the b axis (see text for details). Relative ordering of the chains leads to degenerate domains (a)–(d) belonging to the same irreducible representation Γ^{10} with eigenvectors given in Eq. (A5). Labels 1–16 in (a) indicate the 16 spins in the magnetic unit cell (1–4 label the four atoms in the chemical unit cell shown in Fig. 2). Solid and open circles are Co^{2+} ions with height along the a axis close to 0.25 and 0.75, respectively.

We find that the measured Bragg intensities can be consistently described by an equal population of A and B domains of Γ^{10}. The best fit of the model to the magnetic intensities (for details see the Appendix) is shown in Fig. 5 and in Table I, and gives a good description of the experimental data. A single-domain structure of either A or B type as defined in the Appendix and shown in Fig. 4 is unable to account for the results.

Assuming spin moments confined to the (b,c) plane ($\vartheta_1 = \vartheta_3 = 0$) and equal ordered moments on all sites ($|\mathbf{m}_1| = |\mathbf{m}_3|$) the best-fit results are $\phi_1 = 15(5)°$, $\phi_3 = -15(5)°$, and a fraction of A domain $\alpha = 0.48(3)$ with the sum of discrepancies $\chi^2 = 2.55$. The obtained value for $\alpha \sim \frac{1}{2}$ demonstrates that domains A and B occupy the sample in equal parts. It will be shown in Sec. IV B that those two
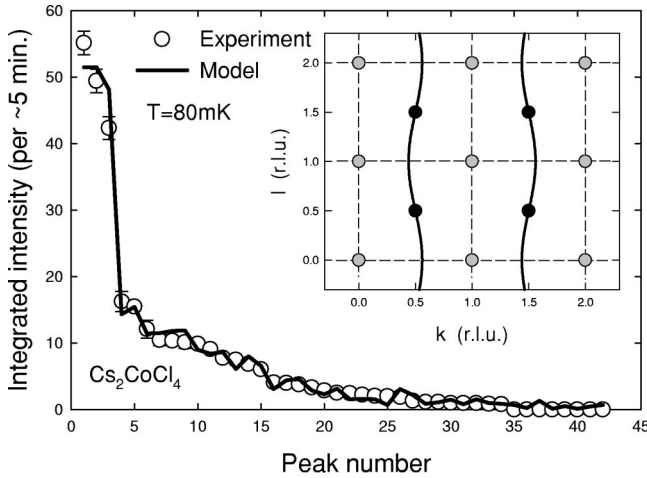
FIG. 5. Experimentally observed integrated magnetic Bragg-peak intensities (open circles) fitted to the model for the magnetic structure described in the text (solid line). Intensity units are the same as in Fig. 3. The horizontal axis indicates the number of the Bragg peaks in the list given in Table I. Inset: Schematic diagram of the (b,c) reciprocal space indicating the positions of magnetic Bragg peaks (solid circles) observed in the present experiment in the ordered phase below $T_N = 217(5)$ mK. Gray circles indicate reciprocal-lattice positions in the (b,c) plane and undulating solid lines mark the positions of the sheets of quasielastic magnetic scattering observed in earlier experiments (Ref. 7) at higher temperatures $(T > 0.3$ K) above the transition to the ordered phase.

domains have the same mean-field exchange energy and are thus expected to occur with the same probability. Taking $\mathbf{m}_1$ out of the (b,c) plane by choosing a series of nonzero values for the out-of-plane angle ϑ_1 and fitting ϑ_3 leads to worse agreement with the observed intensities, so within the accuracy of the experiment it was concluded that magnetic moments are mostly contained in the (b,c) plane.

Figure 6 compares the temperature dependence of the reduced intensity $I/I_{T=80 \text{ mK}}$ of three AF reflections. Here $I_{T=80 \text{ mK}}$ is the observed intensity at base temperature $T = 80$ mK. The three reflections have essentially the same temperature dependence, indicating that the magnetic structure is unchanged between 80 mK and T_N.

B. Magnetic order in applied field

The effect of an applied field on the magnetic order was investigated for fields along a. A spin-flop phase arises [spins cant out of the (b,c) plane towards the field axis] evidenced by a perpendicular antiferromagnetic order coexisting with a ferromagnetic moment along the field direction. Figure 7 shows the field dependence of the $(0,0.5,-1.5)$ reflection measuring the antiferromagnetic component. The intensity increases with increasing field, reaches a maximum around $H \sim 1.4$ T, and then it abruptly drops to zero at $H_c = 2.10(4)$ T in a sharp, near-first-order phase transition. Throughout the spin-flop phase $(0 < H < H_c)$ the ordering wave vector was constant at the commensurate position $(0,\frac{1}{2},\frac{1}{2})$.

The transition at H_c was measured both with increasing and decreasing fields, and no measurable hysteresis effect

TABLE I. Experimentally observed magnetic Bragg-peak intensities compared to the calculated intensities based on the model explained in the text. The magnetic Bragg reflections are in the order of decreasing observed intensity. A visual comparison between experiment and model is made in Fig. 5.

Number	$\mathbf{Q}=(h,k,l)$	Experimental intensity	Calculated intensity
1	(0,0.5,1.5)	55.1(1.8)	51.4
2	(0,-0.5,-1.5)	49.4(1.8)	51.4
3	(0,0.5,-1.5)	42.4(1.7)	44.8
4	(0,-0.5,-4.5)	16.2(1.5)	15.1
5	(0,0.5,-4.5)	15.5(1)	15.5
6	(0,0.5,0.5)	12.1(1.4)	9.7
7	(0,1.5,1.5)	10.4(0.8)	10.1
8	(0,0.5,-0.5)	10.3(0.6)	8.1
9	(0,1.5,-1.5)	10.1(0.9)	8.4
10	(0,-1.5,-4.5)	9.9(0.2)	10.1
11	(0,1.5,-4.5)	9.1(0.2)	8.8
12	(0,-0.5,-3.5)	7.8(0.2)	8.8
13	(0,-0.5,-2.5)	7.5(0.4)	6.0
14	(0,0.5,-3.5)	6.9(0.2)	8.0
15	(0,0.5,-2.5)	6.1(0.2)	6.0
16	(0,0.5,-6.5)	4.1(0.4)	3.5
17	(0,2.5,-4.5)	4.0(0.2)	4.3
18	(0,1.5,-3.5)	3.8(0.4)	4.1
19	(0,-0.5,-6.5)	3.3(0.4)	3.4
20	(0,1.5,2.5)	2.8(0.6)	2.4
21	(0,2.5,-1.5)	2.5(0.4)	2.2
22	(0,3.5,-4.5)	2.4(0.4)	1.8
23	(0,2.5,3.5)	2.2(0.6)	1.9
24	(0,1.5,-0.5)	2.0(0.6)	0.84
25	(0,3.5,-3.5)	2.0(0.6)	0.61
26	(0,2.5,1.5)	1.9(0.4)	3.0
27	(0,1.5,-2.5)	1.3(0.4)	2.0
28	(0,2.5,-2.5)	1.14(0.2)	0.64
29	(0,-0.5,-5.5)	1.14(0.4)	1.2
30	(0,1.5,0.5)	1.0(0.2)	1.1
31	(0,2.5,2.5)	0.95(0.4)	0.8
32	(0,2.5,-3.5)	0.94(0.2)	1.5
33	(0,0.5,-5.5)	0.84(0.3)	1.1
34	(0,2.5,-2.5)	0.79(0.6)	0.64
35	(0,2.5,0.5)	0(0.4)	0.40
36	(0,3.5,0.5)	0(0.4)	0.18
37	(0,3.5,-1.5)	0(0.4)	0.83
38	(0,4.5,-0.5)	0(0.4)	0.08
39	(0,4.5,-1.5)	0(0.4)	0.39
40	(0,4.5,0.5)	0(0.4)	0.09
41	(0,4.5,1.5)	0(0.4)	0.5
42	(0,-1.5,-5.5)	0(0.4)	0.8

was observed as shown in Fig. 7. At 3 T, no AF or incommensurate reflections were observed along the symmetry direction in the (b,c) plane with an intensity larger than 1.5% of the zero-field intensity of the strong $(0,0.5,-1.5)$ reflection, equivalent to half the average background level. The
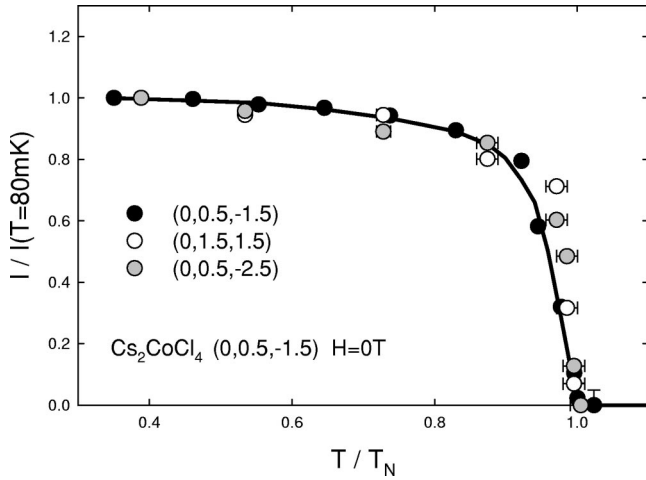
FIG. 6. Zero-field reduced integrated intensity $I/I_{T=80\ mK}$ for three AF Bragg reflections as a function of reduced temperature T/T_N. The solid line is a guide to the eye.

absence of magnetic Bragg peaks in the (b,c) plane suggests that the phase immediately above the critical field H_c is a disordered phase (no LRO) stabilized by the applied magnetic fields, cf. the disordered SL phase in Fig. 1

Figure 8 compares the field dependence of the reduced intensity I/I_0 of three AF reflections at $T=80$ mK, where I_0 is the zero-field integrated intensity. The field dependence coincides showing that the magnetic structure formed by the antiferromagnetic moments in the (b,c) plane is unchanged throughout the spin-flop phase up to the critical field H_c. Furthermore, it shows that the initial increase in the AF Bragg-peak intensities is not due to a rearrangement of the moments in a different spin configuration but arises from an increase in the magnitude of the antiferromagnetically ordered moment. This effect is attributed to the suppression of
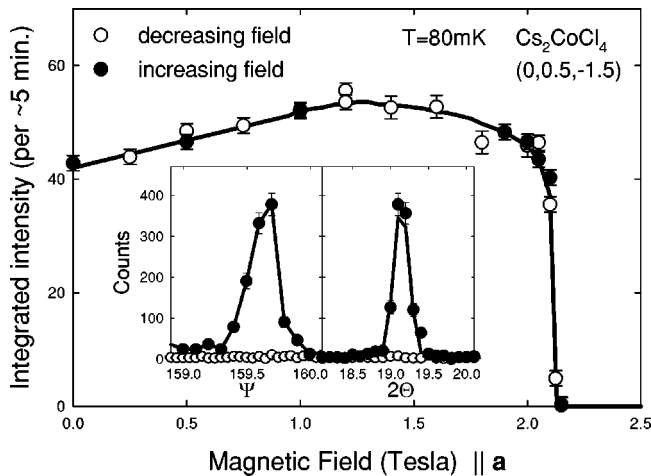

FIG. 7. Integrated intensity of the $(0,0.5,-1.5)$ AF reflection vs applied field at $T=80$ mK. Intensity units are the same as in Table I. The solid line is a guide to the eye. The inset shows the Bragg-peak intensity as a function of Ψ (left) and 2Θ (right) in applied fields below (solid circles) and above H_c (open circles). The solid lines correspond to a fit to the data in the $(\Psi,2\Theta)$ plane as described in the text.
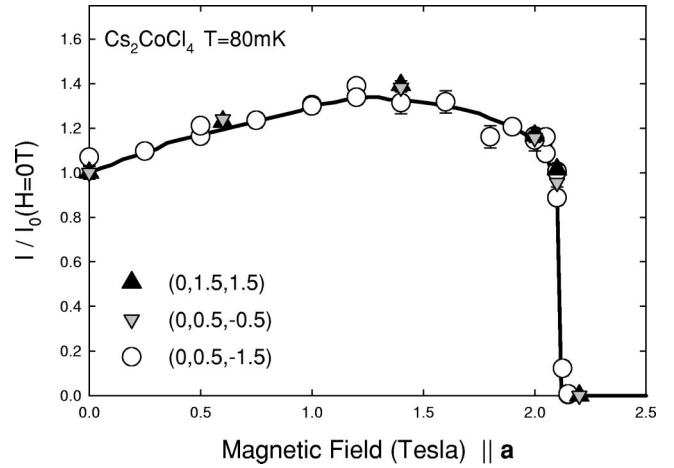

FIG. 8. Reduced integrated magnetic Bragg-peak intensity, I/I_0, as a function of field for three AF reflections at $T=80$ K. The data for $(0,1.5,1.5)$ and $(0,0.5,-0.5)$ were measured with increasing field, while most of the data for $(0,0.5,-1.5)$ were measured with decreasing field as shown in Fig. 7. The solid line is a guide to the eye.

zero-point quantum fluctuations by the applied field which allows more of the available spin moment to order.

The effect of the applied field initially suppressing fluctuations and stabilizing the antiferromagnetic order is even more pronounced at elevated temperatures where the zero-field moment value is further reduced by thermal fluctuations. Figure 9 shows that the antiferromagnetic moment increases significantly in applied field to reach a maximum around 1.4 T and only at much higher fields it collapses in a sharp transition at $H_c=2.10(4)$ T (nearly T independent up to 195 mK$=0.9T_N$).

Consistent with the above observation, scans in temperature at intermediate fields (below H_c) observe that the transition temperature is higher than in zero field, as expected for a structure with an increased ordered moment (stabilized by the field) that has a larger mean-field energy and is thus more
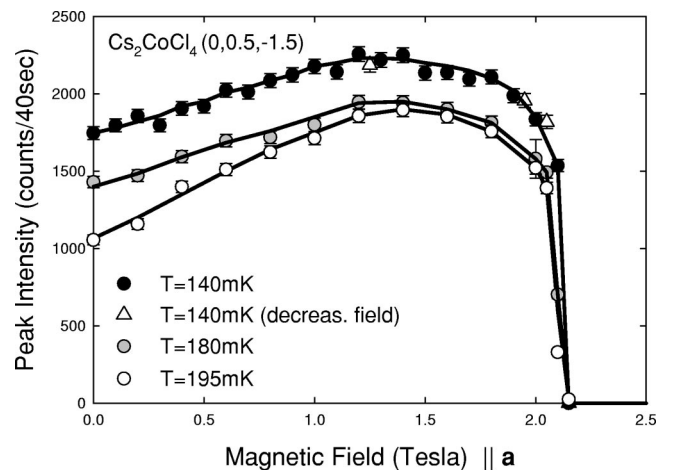

FIG. 9. Peak intensity of the $(0,0.5,-1.5)$ AF reflection vs applied field at three different temperatures. Intensity units are the same as in Fig. 10. The solid lines are guides to the eye.
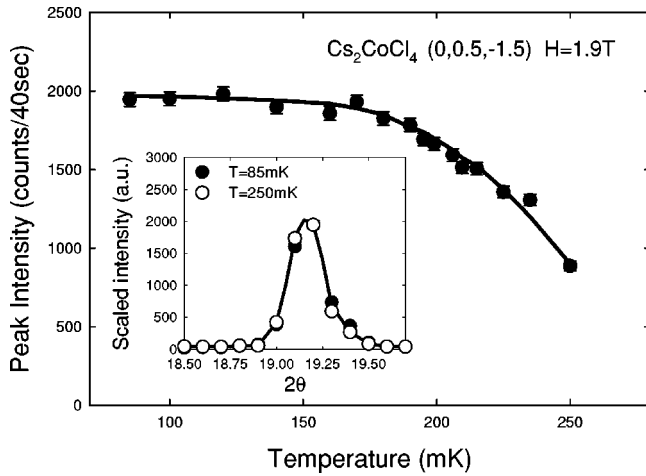
FIG. 10. Peak intensity of the $(0,0.5,-1.5)$ AF reflection vs temperature in fixed applied field $H=1.9$ T. Intensity units are the same as in Fig. 9. The solid line is a guide to the eye. Inset: observed intensity of the $(0,0.5,-1.5)$ reflection as a function of scattering angle 2Θ at two temperatures $T=80$ and 250 mK. The 250 mK data were scaled to match the peak intensity of the 80 mK data for direct comparison. The solid line is a Gaussian fit.

stable against thermal fluctuations. This is shown in Fig. 10 by measurements of $(0,0.5,-1.5)$ peak intensity in a field of $H=1.9$ T. The intensity decreases more slowly with increasing temperature than in zero field (see Fig. 3) and the order is stable beyond the zero-field transition temperature $T_N=217(5)$ mK and disappears only at much higher temperatures above the range covered by this experiment, extrapolated to $T_N(H=1.9$ T$)\sim300(20)$ mK. The long-range coherence of the structure is unchanged in the whole measured temperature range as evidenced by the same angular width of 2Θ scans at the two extreme temperatures shown in the inset of Fig. 10.

C. Temperature-field phase diagram

In Fig. 11 we show an $(H\|a,T)$ phase diagram of Cs_2CoCl_4 based on the measurements described above. At zero field, Cs_2CoCl_4 orders below $T_N=217(5)$ mK with a commensurate wave vector $\mathbf{k}=(0,\frac{1}{2},\frac{1}{2})$. The chains are ordered antiferromagnetically along their length and the moments are contained in the (b,c) plane at a small angle with the b axis. Magnetic fields applied along the a axis initially stabilize the antiferromagnetic order by suppressing fluctuations. This is directly observed both in the increase of the perpendicular antiferromagnetic moment in applied field (see Figs. 8 and 9) and also in the increase in the transition temperature at finite field (compare Figs. 3 and 10). At higher fields the order becomes unstable and above H_c $=2.10(4)$ $T\|a$ it collapses in a sharp, near-first-order transition to a phase with no long-range magnetic order in the (b,c) plane, possibly a spin-liquid phase. Based on (i) the absence of order in the (b,c) plane, (ii) nonsaturation of the magnetization, see Sec. III D, and (iii) the expected order-disorder transition driven by the large fluctuations arising from field noncommutation, we identify the phase above the
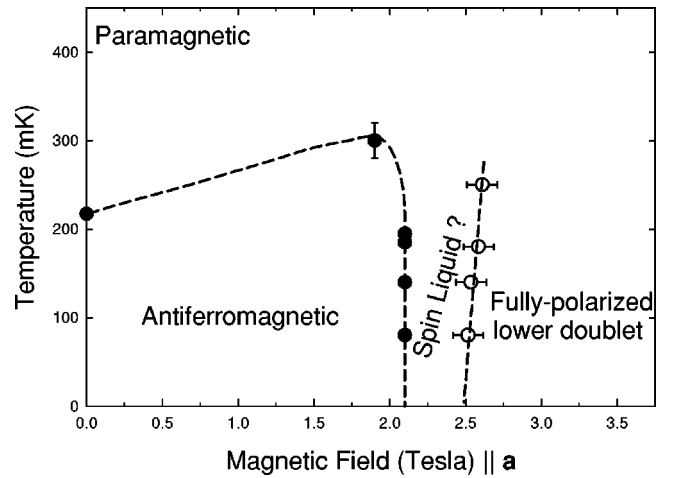
critical field H_c with the spin-liquid (SL) state predicted to occur below saturation in Fig. 1.

D. Ferromagnetic moment as a function of field

The ferromagnetically ordered moment was determined from the intensity of the (011) reflection. The resulting magnetization curve at $T=80$ mK is shown in Fig. 12. The ferromagnetic moment increases over the whole range of the

FIG. 11. Schematic magnetic phase diagram of Cs_2CoCl_4 as a function of magnetic field and temperature. Solid symbols denote transitions where the AF LRO in the (b,c) plane disappears, see Figs. 3 (10) and 7 (8). Open symbols mark crossover fields in the magnetization curve (see Fig. 13) identified with near-saturation of the lower-doublet magnetization. Dashed lines are guides, to the eye.
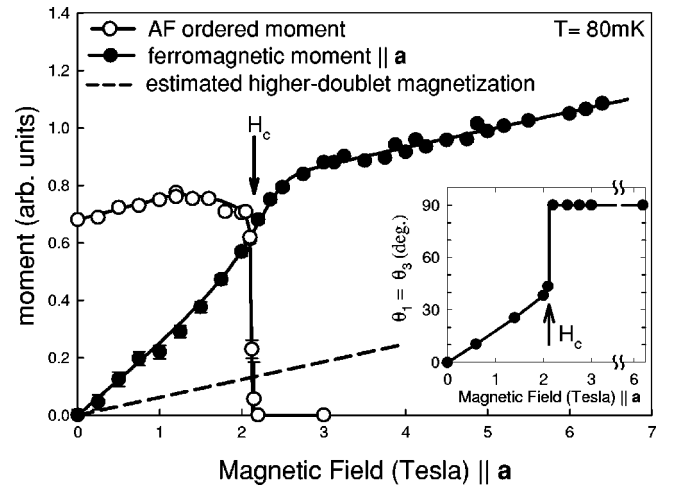

FIG. 12. Ordered moments as a function of applied field along a at $T=80$ mK. Open circles show the perpendicular ordered moment and solid symbols indicate the ferromagnetic ($\|a$) component. The solid lines are guides to the eye and the dashed line shows the estimated partial contribution to the magnetization due to polarizing the higher-doublet states alone, assuming a constant susceptibility vs field. The inset shows the canting angle θ made by the total ordered moment with the (b,c) plane (above $H_c=2.1$ T it is assumed that the spin components perpendicular to the field axis are not ordered and therefore $\theta=90°$).
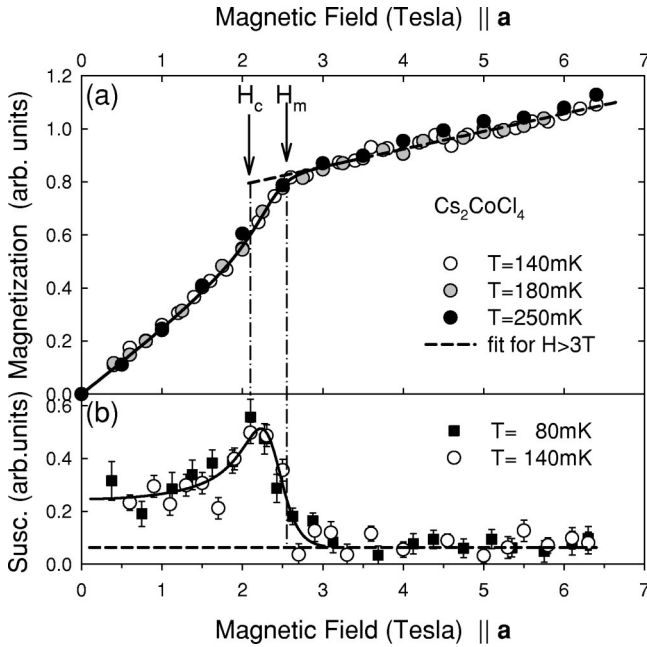
FIG. 13. (a) Magnetization vs field along the a axis at various temperatures $T = 140$, 180, and 250 mK. The solid line is a guide to the eye and the sloping dashed line shows a fit to linear behavior at fields above ~ 3 T. (b) Susceptibility vs field at $T = 80$ and 140 mK. The solid line is a guide to the eye (the horizontal dashed line shows the approximated partial contribution from the higher-doublet states). H_c is the critical field where the antiferromagnetic order in the (b,c) plane disappears and H_m is the crossover field above which the magnetization has approached high-field near-linear behavior.

measurements up to 6.4 T and two regimes can be identified: a low- and a high-field region separated by a crossover around $H_m = 2.52 \pm 0.06$ T above which the rate of increase of the magnetization is significantly reduced. This crossover is best illustrated in a plot of the differential susceptibility ($\chi = \partial M / \partial H$) in Fig. 13(b) which shows significantly reduced values above H_m (of order 4 ± 1 compared to zero field). This crossover behavior is typical of spin-$\frac{3}{2}$ systems with two energetically separated Kramers doublets (for details see Sec. IV D): in applied field the lower-lying doublet is saturated first at a field H_m above which the magnetization curve shows a large decrease in susceptibility as only higher-doublet states can still be polarized.

The crossover field H_m (defined experimentally as the field where the magnetization is within less than 5% of the linear high-field behavior) is plotted in Fig. 11 (open symbols). Note that the antiferromagnetic order in the (b,c) plane is suppressed at $H_c = 2.10(4)$ T much below the lower-doublet saturation field identified with $H_m = 2.52 \pm 0.06$ T ($T = 80$ mK). The absence of long-range order for $H_c < H < H_m$ is not due to thermal fluctuations as this field range remains finite after extrapolation to $T = 0$ as shown in Fig. 11. This region is thus a quantum disordered phase induced by the applied field and is thus consistent with the proposed spin-liquid phase in the schematic phase diagram in Fig. 1.

IV. DISCUSSION

In the previous section we have established the magnetic structure of Cs_2CoCl_4 and the effects of a noncommuting field on its ground state. Here we discuss relevant microscopic mechanisms that may give rise to the observed ordered structure and find that a simple (nearest-neighbor) mean-field picture cannot explain all observed features. We then estimate the ordered moment and find a significant reduction from the available moment, indicating the presence of strong quantum fluctuations. Finally, we relate the observed magnetic phase diagram to the minimal model of the XY chain in a noncommuting field.

A. Commensurate vs incommensurate order

The observed ordering wave vector condenses out of the diffuse scattering measured by Yoshizawa *et al.*[7] in the disordered phase at 0.3 K just above T_N (inset of Fig. 5), consistent with the expectation that order should arise at wave vectors where paramagnetic fluctuations are strong. The measured diffuse scattering[7] showed systematic incommensurate modulations along the chain direction attributed to competing interchain interactions. In isotropic systems, a mean-field picture for such frustrated couplings would predict incommensurate, spiral spin order along the chains.[7] The observed order, however, occurs at the commensurate, antiferromagnetic wave vector $\mathbf{k} = (0, \frac{1}{2}, \frac{1}{2})$ where interchain frustration effects cancel out and chains behave as decoupled.

In Cs_2CoCl_4 the tendency to form spiral order is suppressed because XY planes of neighboring chains are not parallel but make a large relative angle 2β resulting in an Ising-like frustrated interchain coupling between the XY-like 1D chains. Considering only chains 1 and 4 in the chemical unit cell with XY spins, the energy of a helical order in the easy planes of the two chains at a pitch to minimize frustration for the b-axis spin components is $E_{helix} = S^2[-J - |\cos 2\beta| J_{bc}^2 / (2J)]$. This spiral structure becomes degenerate with the simple AF Néel order (spins along b) in the limit of orthogonal easy planes $2\beta = 90°$ (close to the actual situation in Cs_2CoCl_4). In the proximity of this limit of small effective frustration other effects may stabilize the observed commensurate Néel-type order and possibilities include the following: (i) zero-point quantum fluctuations could introduce nonlinear terms in the free-energy expansion which may lift the classical degeneracy and promote ordering at the decoupling point $\mathbf{k} = (0, \frac{1}{2}, \frac{1}{2})$, (ii) further neighbor couplings such as between sites 1 and 5, or 1 and 6, although believed to be small, could potentially stabilize the antiferromagnetic order, and (iii) other effective Ising-type anisotropies arising from spin-orbit coupling or crystal-field effects may favor spin ordering close to the b axis with the lowest energy achieved for an antiferromagnetic-type arrangement (constant moment on each site) as opposed to other incommensurate structures. We have also considered dipolar couplings and found an increased energy by 10^{-5} meV per spin for the observed order compared to a ferromagnetic-type arrangement along the c axis and thus it was concluded that dipolar effects could not explain the observed structure.

B. Mean-field analysis

To identify the exchange couplings involved in stabilizing the observed magnetic structure we calculate its energy in the mean-field approximation. We find simple energetic arguments to explain (i) why the observed magnetic structure belongs to the Γ^{10} irreducible representation, (ii) why the ordered moments are confined to the (b,c) plane, and (iii) why a multidomain structure occurs.

We first assume an isotropic Heisenberg exchange such that the three spin components along x, y, and z (a, b, and c directions) could be treated separately. The observed ordering wave vector $\mathbf{k}=(0,\frac{1}{2},\frac{1}{2})$ indicates a doubling of the unit cell along the b and c axes leading to 16 different magnetic sublattices in the magnetic unit cell, as shown in Fig. 4(a). Using this extended unit cell we calculated the interaction matrix η in the mean-field approximation; the eigenvectors of η are basis vectors of the magnetic ordering and the eigenvalues are the corresponding energy levels. Diagonalization of η gives the two lowest-energy levels $\lambda_{\pm}=-J\pm J_{ac}$, assuming weakly coupled AF chains running along the b axis ($J>0$ and $J\gg J_{ab},J_{ac},J_{bc}$). For AF exchange between spins 1 and 2 ($J_{ac}>0$) the ground state has energy $\lambda_{-}=-J-J_{ac}$ and there are three degenerate eigenvectors: (i) ordering of the $y(b)$ spin components in the irreducible representation Γ^{10} [Eq. (A5)], (ii) ordering of the $z(c)$ components also in Γ^{10}, or (iii) ordering of the $x(a)$ components in Γ^9 [Eq. (A4)].

Upon including anisotropy effects this threefold degeneracy is lifted favoring ordering along the b axis (b is a common easy axis for all spins as shown by paramagnetic-susceptibility measurements[11,12]). The determined magnetic structure shown in Fig. 4 is indeed in the Γ^{10} representation with the largest spin moment along the easy b axis and a small moment along c, also in Γ^{10}. The observed confinement of the ordered moments to the (b,c) plane can also be understood on energetic grounds: according to Eq. (A5) ordering of spins along a in Γ^{10} would have parallel spins on sites 1 and 2, which would be energetically unfavored by the AF interchain couplings J_{ac} (the ordering of the a components cannot belong to another representation, say, Γ^9, because the full Hamiltonian including all anisotropy terms respects the symmetry of the crystal structure and therefore does not mix spin orderings from different irreducible representations).

For a magnetic ordering of the b- and c-spin components in the Γ^{10} representation the spin configuration is not unique, but instead four distinct domains are possible, all with the same mean-field exchange energy. Those four domains are shown in Fig. 4 and the degeneracy arises because the Γ^{10} representation of the b and c components is two dimensional (sites 1 and 3 are independent).

Interestingly, at the mean-field level the ground-state energy does not depend on the couplings between sublattices (1,2) and (3,4). This is a general result for any antiferromagnetic ordering along b, i.e., $\mathbf{k}=(0,\frac{1}{2},l)$ as can be easily seen by inspecting Fig. 4(a): each spin on the second group of sublattices interacts with pairs of antiparallel spins from the first group such that the net interactions cancel out. For ex-

ample, spin 4 interacts through J_{bc} with the pair of antiparallel spins 1 and 9 (5 and 13). Similarly, spin 4 at $x\sim0.25$ interacts through J'_{ab} with the pair of antiparallel spins 6 and 14 at $x\sim0.75$ (J_{ab} with antiparallel spins 6 and 14 at $x\sim-0.25$).

The observed ordering at $\mathbf{k}=(0,\frac{1}{2},\frac{1}{2})$ thus consists of two interpenetrating magnetic lattices that are noninteracting at the mean-field level. One lattice contains atoms 1, 2, 5, 6, 9, 10, 13, and 14, and the other has atoms 3, 4, 7, 8, 11, 12, 15, and 16 in the magnetic unit cell. Since those two global lattices are related by inversion symmetry ($\bar{1}$ at the center of the chemical unit cell) the intrasublattice interactions are identical and so the ordered magnetic moment is expected to be the same for both, as assumed in the analysis of the magnetic Bragg peaks in Sec. III that gave good agreement with the experiment.

The observed small alternating tilt $\phi=\pm15(5)^{\circ}$ of the magnetic moments away from the b axis indicates an effective local spin anisotropy. We do not have an explanation for its origin but propose that it may arise when the Heisenberg interchain exchange between sites with rotated XY planes (such as J_{ac} between spins 1 and 2 in Fig. 2) is projected onto the lower-lying Kramers doublet of effective spin $\frac{1}{2}$.

C. Absolute magnitude of the ordered moment

The magnitude of the ordered moment at $T=80$ mK was determined by comparing the nuclear and the AF Bragg-peak intensities (see the Appendix, Sec. 3). Using $A_{\exp}$ and Eq. (A6) the resulting ordered moment at $T=80$ mK is $m_0=1.7(4)\mu_B$ (zero field).

The lower-lying Kramers doublet of Co^{2+} ions with effective spin $\frac{1}{2}$ has anisotropic g values, $g_{x,y}=2g$ and $g_z=g$. Here $g=2.4$ is the isotropic g value of the underlying spin $\frac{3}{2}$ and was determined from high-temperature paramagnetic-susceptibility measurements.[16,10,15] This implies that the available moment in the XY plane is $g_{x,y}\mu_B/2=2.4\mu_B$. From the present diffraction experiments the estimated ordered moment along the in-plane axis b common to all spins is $m_0\cos\phi=1.6(4)\mu_B$, clearly smaller than the available full moment in the XY plane (the ordered moment along the c axis is very small and is a mixture of longitudinal and transverse parts). The reduction of the ordered moment from the full available value indicates strong zero-point fluctuations in the ground state.

D. Magnetization curve

In this section we consider a minimal magnetic Hamiltonian consistent with the crystal field and magnetization data on Cs_2CoCl_4, and relate the observed magnetic phase diagram to the phenomenology of anisotropic magnets in noncommuting fields. We analyze the magnetization curve in terms of a spin-$\frac{3}{2}$ Hamiltonian appropriate for the Co^{2+} ions and identify the observed crossover at H_m with near-saturation of the lower-lying spin doublet. We then estimate the lower-doublet magnetization curve (Fig. 14) and discuss it in terms of an effective $S=\frac{1}{2}$ XXZ Hamiltonian in noncommuting field.
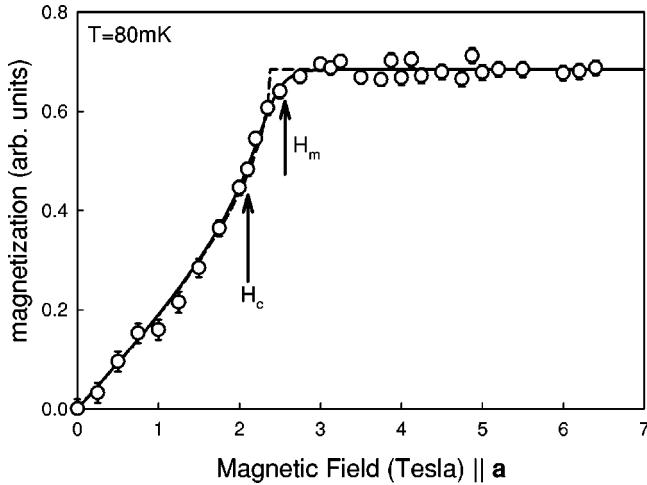
FIG. 14. Partial magnetization from lower-doublet states alone as a function of applied field along a. The data is obtained from the observed total magnetization by subtracting an estimate of the higher-doublet contribution as indicated in Fig. 12 (dashed line) and described in the text. $H_c = 2.1$ T is the critical field where the antiferromagnetic order in the (b,c) plane is suppressed (see Fig. 7) and H_m is the crossover field above which the (lower-doublet) magnetization is nearly (within 5%) saturated. The solid line is a fit to the generic form in Eq. (5) (the dashed line shows this calculation at zero temperature) as described in the text.

1. Full Hamiltonian

A minimal Hamiltonian for the spin $\tilde{S} = \frac{3}{2}$ Co^{2+} ions that includes the 1D exchange and crystal-field effects is

$$\tilde{\mathcal{H}} = \sum_i I\tilde{\mathbf{S}}_i \cdot \tilde{\mathbf{S}}_{i+1} + D(\tilde{S}_i^z)^2 - g\mu_B H_z \tilde{S}_i^z - g\mu_B H_x \tilde{S}_i^x, \quad (4)$$

where I is the nearest-neighbor (isotropic) exchange interaction along the 1D chains and D is the easy-plane anisotropy energy (perpendicular to the local z axis). The last two terms in Eq. (4) are the Zeeman energy in longitudinal ($H_z = H \sin \beta$) and transverse ($H_z = H \sin \beta$) fields, where β is the angle between the field direction and the XY plane (for $H \| a$ this is equal to the angle between the local z axis and the c axis in Fig. 2). In the absence of magnetic fields ($H = 0$) and in the limit of large local anisotropy ($D \gg I$) only the lower-lying doublet $|\pm\frac{1}{2}\rangle$ contributes to the low-energy dynamics and in this subspace the degrees of freedom can be described[8] by an effective spin $S = \frac{1}{2}$ XXZ Hamiltonian [Eq. (2)] with an exchange $J = 4I$ and anisotropy parameter $\Delta = 0.25$.

2. XXZ chain in a longitudinal (commuting) field

The physics of the XXZ model [Eq. (2)] is well understood in the limit $\Delta = 0$ when it is equivalent to a 1D free fermion gas. Longitudinal fields ($H \| z$) act as chemical potentials filling up the quasiparticle band. The magnetization is directly related to the filling factor and at finite temperature T is given by[9]

$$M(H,T) = \frac{M_{1z}}{\pi} \int_0^\pi d\omega \tanh \frac{g_z \mu_B (H - H_{1z} \cos \omega)}{2 k_B T}, \quad (5)$$

with the $T = 0$ result $M(H) = 2M_{1z} \sin^{-1}(H/H_{1z})/\pi, H \leqslant H_{1z}$. Figure 14 shows a typical magnetization curve plot at $T = 0$ (dashed curve) and finite T (solid line) where the approach to saturation is rounded off by thermal fluctuations. The saturation magnetization $M_{1z} = g_z \mu_B/2$ (per spin) is reached at the critical field (for finite Δ) $H_{1z} = J(1 + \Delta)/g_z \mu_B$. The zero-field, $T = 0$ longitudinal susceptibility is reduced compared to the semiclassical value due to quantum fluctuations and for $\Delta = 0.25$ is calculated as[17] $\chi_z(0) \simeq 0.237 g_z^2 \mu_B^2/J$. Using the proposed values for the exchange interactions in Cs_2CoCl_4, $J = 0.23(1)$ meV and $g_z = 2.4$, the longitudinal critical field is estimated as $H_{1z} = 2.1(1)$ T.

3. XXZ chain in a transverse (noncommuting) field

Transverse fields ($H \| x$) have a very different effect compared to longitudinal fields because they (i) break the spin rotational symmetry from U(1) to Ising, and (ii) do not commute with the exchange terms. In low fields this produces perpendicular long-range antiferromagnetic order (spin-flop phase).[5,6] The noncommutation of the field introduces fluctuations that become strong enough above a critical field to suppress the antiferromagnetic order and induce a transition to a spin-liquid state where the spin moment is not yet saturated along the field and the finite perpendicular spin components have exponentially decaying correlations. A typical ground-state phase diagram is shown in Fig. 1. The critical disordering field is estimated[6] at $H'_{1x} \simeq J(3 + \Delta)/2g_x \mu_B$ whereas exact diagonalizations of finite chains[5] suggest that near saturation of the magnetization occurs at much higher fields, similar to the classical saturation value $H_{1x} = 2J/g_x \mu_B$. For Cs_2CoCl_4 those estimates give $H'_{1x} \simeq 1.3(1)$ T and $H_{1x} = 1.7(1)$ T. The zero-field, $T = 0$ susceptibility is again reduced compared to the semiclassical value due to quantum fluctuations and for the XY chain is calculated as[17] $\chi_x(0) \simeq 0.075 g_x^2 \mu_B^2/J$.

4. Full Hamiltonian in a longitudinal field

For the $\tilde{S} = \frac{3}{2}$ Hamiltonian in Eq. (4) with well-separated energy scales for the lower $|\pm\frac{1}{2}\rangle$ and higher $|\pm\frac{3}{2}\rangle$ doublets, a crossover in behavior is expected in applied magnetic field from a low-field region where only the lower doublet participates (or both doublets, depending on the field direction) to a higher-field region where the lower doublet is saturated and only the higher doublet contributes to the magnetization.

Longitudinal fields ($H \| z$) do not mix higher-doublet states until very large fields of the order of the interdoublet separation energy $H_{2z} \simeq 2D/g_z \mu_B$. At low fields only the lower-doublet states contribute and the physics is that of the XXZ model in longitudinal fields. Above the lower-doublet saturation at H_{1z} the magnetization shows a plateau at $M_{1z} = g_z \mu_B/2$ (per spin), stable up to fields around H_{2z} when the magnetization increases again by mixing in states from the higher-lying doublet $|\pm\frac{3}{2}\rangle$ to finally reach the full spin value

of $3/2g\mu_B$. The upper longitudinal critical field for Cs_2CoCl_4 is estimated at $H_{2z}=9(1)$ T.

5. Full Hamiltonian in a transverse field

Transverse fields ($H\|x$) in Eq. (4) have finite matrix elements between the two doublets and thus mix higher-doublet states into the ground state (of order $g\mu_B H/2D$) at any finite field.[16] Both doublets participate at low fields (large susceptibility) and above a crossover field the lower doublet is near saturated and only the higher doublet contributes (small susceptibility). Such a behavior is evident in earlier magnetization measurements[16,12] on Cs_2CoCl_4 in fields along the b axis (entirely transverse) where the magnetization increases rapidly at low fields with a large susceptibility, then crosses over above ~ 3 T to a region where the magnetization increases much slower to approach saturation ($3.6\mu_B$) at fields >16 T.

6. Comparison with the observed (total) magnetization

The a-axis magnetization shown in Fig. 12 is in broad agreement with the expected behavior for mixed longitudinal and transverse fields on the full $\widetilde{S}=\frac{3}{2}$ Hamiltonian in Eq. (4): a rapid increase is observed at small fields (both doublets contribute) followed by a crossover to a much slower increase at higher fields (only higher-doublet states contribute). The crossover field $H_m=2.52\pm0.06$ T ($T=80$ mK) is identified with near-saturation of the lower doublet. This field appears to be larger than the estimated near- or full-saturation fields for purely transverse H_{1x} or purely longitudinal fields H_{1z}, possibly due to either the approximations used in estimating H_{1x} solving Eq. (4) assuming decoupled lower and higher doublets, or other terms in the Hamiltonian, such as interchain exchanges not included explicitly here.

Figure 14 shows the partial lower-doublet magnetization assuming the contribution to the magnetization from the higher-doublet states can be approximated by a constant susceptibility (as shown in Fig. 12). This assumption is consistent with calculations in the single-site approximation following Ref. 16, which predict that the higher-doublet susceptibility for fields tilted at $\beta=45°$ is relatively small [compared to $\chi_{x,z}(0)$ of the lower doublet] and decreases smoothly by only $\sim 25\%$ between zero and 5 T. Putting the magnetization values in Fig. 14 on an absolute scale gives a lower-doublet saturation moment $M_s=1.7(4)\mu_B$, consistent with typical values expected for fields applied at an angle to the z axis $M_s=\sqrt{g_x^2\cos^2\beta+g_z^2\sin^2\beta}\mu_B/2\simeq1.9\mu_B$ for $\beta=45°$.

7. (Partial) magnetization of the XXZ chain

Since no detailed predictions are available for the magnetization curve of XXZ chains in mixed longitudinal and transverse fields we compare the results with the generic analytic form given in Eq. (5). This is valid strictly only for XY chains in longitudinal fields, but it provides a simple analytic

form to parametrize the data and extract an effective saturation field H_s, the saturation magnetization, and an effective "temperature" $\widetilde{T}$, which is a measure of the fluctuations causing the rounded approach to saturation.

The extracted saturation field $H_s=2.37(3)$ T ($80<T<250$ mK) is significantly larger than the critical field $H_c=2.10(4)$ T where the antiferromagnetic order disappears, giving further support for the existence of an intermediate phase between the antiferromagnetic order and the nearly fully polarized phase as indicated in the phase diagram in Fig. 11. The fitted "temperatures" $\widetilde{T}$ are systematically larger than the true measuring temperatures T [$\widetilde{T}=200(50)$ mK for the $T=80$ mK data, fit shown by solid line in Fig. 14] indicating more fluctuations in the system than can be accounted for by temperature alone. A source of those fluctuations can be the noncommuting fields that create disorder effects at large fields. At small noncommuting fields the dominant effect is breaking the spin rotational symmetry which has the consequence of promoting long-range order in a spin-flop phase. This is also in agreement with the experiments, which observed that low fields stabilize the perpendicular antiferromagnetic order.

E. Further studies

The measurements presented here have highlighted a potentially very significant field-induced phase transition in Cs_2CoCl_4. The field dependence of the order correlates well with the expectations of a quantum magnet driven through a quantum critical point by a noncommuting field. Essential to this picture is the identification of the disordered phase with a gapped spin-liquid state. Further studies using NMR, magnetic susceptibility, and heat capacity are called for to investigate whether a spin gap really does open above the critical field of 2.10 T. It would also be very interesting to look for any evidence of spin-glass behavior induced by the field. Inelastic neutron-scattering measurements of the excitations in a field should be particularly revealing and we plan to make such measurements in the near future.

V. CONCLUSIONS

In conclusion, single-crystal neutron diffraction was used to determine the magnetic ordering as a function of noncommuting applied field in the quasi-1D spin-$\frac{1}{2}$ XY-like antiferromagnet Cs_2CoCl_4. In zero field long-range order with wave vector $\mathbf{k}=(0,\frac{1}{2},\frac{1}{2})$ was found below $T_N=217(5)$ mK. The magnetic structure was determined using group theory and has spins ordered antiferromagnetically along the chains with moments confined to the (b,c) plane. A domain structure was found with adjacent chains in different phases. Possible mechanisms promoting this commensurate order were discussed. The observed reduction in the ordered moment was attributed to zero-point fluctuations in the ground state.

Magnetic fields applied along the a axis were found to initially stabilize the perpendicular AF order and form a spin-

TABLE II. Irreducible representation of the group $G_\mathbf{k}$.

	1	1^t	2_x	2_x^t	$\bar{1}/\bar{1}^t$	$2_y/2_y^t$	$2_z/2_z^t$	m_{xy}/m_{xy}^t	m_{xz}/m_{xz}^t	m_{yz}/m_{yz}^t
Γ^1	1	1	1	1	1	1	1	1	1	1
Γ^2	1	1	1	1	-1	-1	1	1	-1	-1
Γ^3	1	1	1	1	-1	1	-1	-1	-1	1
Γ^4	1	1	1	1	1	-1	-1	-1	1	-1
Γ^5	1	1	-1	-1	1	1	-1	1	-1	-1
Γ^6	1	1	-1	-1	1	-1	1	-1	-1	1
Γ^7	1	1	-1	-1	-1	1	1	-1	1	-1
Γ^8	1	1	-1	-1	-1	-1	-1	1	1	1
Γ^9	2	-2	-2	2	0	0	0	0	0	0
Γ^{10}	2	-2	2	-2	0	0	0	0	0	0

flop phase. This structure becomes unstable at high fields where a transition occurs to a phase with no LRO in the (b,c) plane. Measurements of the ferromagnetic component found that near-saturation of the moments occurs only at much higher fields. The phase between the spin-flop and saturated phases $2.10 < H_{SL} < 2.52$ T $\|a$ has been proposed to be a spin-liquid state disordered by the strong quantum fluctuations arising from the applied field noncommutability with the exchange Hamiltonian.

APPENDIX

1. Group-theory analysis

Using the space-group symmetry of the crystal structure we identify allowed basis vectors for a magnetic structure with the observed wave vector $\mathbf{k}=(0,\frac{1}{2},\frac{1}{2})$. This is done by determining the irreducible representations and eigenvectors of the little group $G_\mathbf{k}$ of symmetry operations that leave the wave vector $\mathbf{k}$ invariant.

We start by considering the symmetry elements of the *Pnma* space group of Cs_2CoCl_4:

$$\{1,\bar{1},2_x,2_y,2_z,m_{xy},m_{xz},m_{yz}\}, \qquad (A1)$$

where 1 is the identity operator, $\bar{1}$ is the inversion at the origin, 2_α denotes a 180° screw axis along directions $\alpha = x$, y, or z (180° rotation followed by a translation with half a unit cell along axis α), and where throughout this group-theory section the axes x, y, and z refer to the crystallographic directions a, b, and c. $m_{\alpha\beta}$ is a glide plane containing axes α and β. The group is nonsymmorphic because the group elements $\{R|\mathbf{a}\}$ consist of an operation R followed by a translation $\mathbf{a}$ equal to half a direct lattice vector. The experimentally observed ordering wave vector $\mathbf{k}=(0,\frac{1}{2},\frac{1}{2})$ is invariant under all these operations such that the little group $G_\mathbf{k}$ contains all of the above elements.

The representations of the little group $G_\mathbf{k}$ are given by $\exp(-i\mathbf{ka})\Gamma^\alpha(R_\mathbf{k})$. The ordering in Cs_2CoCl_4 is a special case because the crystal symmetry is nonsymmorphic and the ordering wave vector lies on the Brillouin-zone boundary. The representations of elements $R_\mathbf{k}$ of the space group with subsequent translation $\mathbf{t}=(0,n,m)$ such that $n+m$ = odd have a different sign to those of operations $R_\mathbf{k}$ alone, and this leads to additional irreducible representations. They can be found by adding new group elements to the little group $G_\mathbf{k}$,[18] which are the original elements with an additional translation $\mathbf{t}$. We call the additional translations

$$\{1^t,\bar{1}^t,2_x^t,2_y^t,2_z^t,m_{xy}^t,m_{xz}^t,m_{yz}^t\}. \qquad (A2)$$

Thus the little group $G_\mathbf{k}$ consists of a total of 16 elements. We determined the classes and the character table of this group and these are shown in Table II. The group consists of ten different classes and therefore has ten irreducible representations. Only two of the representations fulfill the necessary condition that $\chi(1)=-\chi(\bar{1}^t)$ (this condition follows directly from the prefactor of the representation which changes sign under a translation by $\mathbf{t}$). The experimentally observed ordered magnetic structure is thus associated with one of these two representations.

The eigenvectors ϕ^λ of the irreducible representations Γ^λ were determined using the projector method.[18] They are given by

$$\phi^\lambda = \sum_g \chi^\lambda(g) g(\phi), \quad \lambda = 1 \cdots 10, \qquad (A3)$$

where g is an element of the little group and ϕ is any vector of the order-parameter space. For $\mathbf{k} = (0,0.5,0.5)$ the magnetic unit cell is doubled along the b and c axes, and the order-parameter space is a 48-dimensional axial vector because the magnetic unit cell contains 16 magnetic moments as indicated in Fig. 4(a) and each has three space components. We obtain

$$\phi^9 = (m_{1x}, m_{1y}, m_{1z}, -m_{1x}, m_{1y}, m_{1z},$$

$$m_{3x}, m_{3y}, m_{3z}, -m_{3x}, m_{3y}, m_{3z},$$

$$-\mathbf{m}_1, -\mathbf{m}_2, -\mathbf{m}_3, -\mathbf{m}_4,$$

$$-\mathbf{m}_1, -\mathbf{m}_2, -\mathbf{m}_3, -\mathbf{m}_4,$$

$$\mathbf{m}_1, \mathbf{m}_2, \mathbf{m}_3, \mathbf{m}_4) \qquad (A4)$$

for representation Γ^9. $m_{i\alpha}$ is the component α of the magnetic moment i with $1 \leq i \leq 16$. For better readability, in the above equation the individual components of the magnetic moments 5 to 16 were omitted and the magnetic moments were written as vectors, i.e., $\mathbf{m}_5 = -\mathbf{m}_1 = (-m_{1x}, -m_{1y}, -m_{1z})$. For representation Γ^{10} we obtain

$$\phi^{10} = (m_{1x}, m_{1y}, m_{1z}, m_{1x}, -m_{1y}, -m_{1z},$$

$$m_{3x}, m_{3y}, m_{3z}, m_{3x}, -m_{3y}, -m_{3z},$$

$$-\mathbf{m}_1, -\mathbf{m}_2, -\mathbf{m}_3, -\mathbf{m}_4,$$

$$-\mathbf{m}_1, -\mathbf{m}_2, -\mathbf{m}_3, -\mathbf{m}_4,$$

$$\mathbf{m}_1, \mathbf{m}_2, \mathbf{m}_3, \mathbf{m}_4). \qquad (A5)$$

The ordered magnetic structure is thus doubly degenerate in each of the three spin components given by the dimension two of these two representations.

A magnetic structure in the Γ^{10} irreducible representation can occur in several different domains. Assume spins are confined to the (b,c) plane in a typical configuration shown in Fig. 4(a) called domain A1. One can construct domain A2 in Fig. 4(c) by reversing the $b(y)$ components of all spins and keeping the $c(z)$ components unchanged. Domain B1 in Fig. 4(b) is obtained from domain A1 by reversing the spins on sites 3 and 4 (and 7, 8, 11, 12, 15, 16) and using the same rule one transforms domain A2 in Fig. 4(c) into B2 in Fig. 4(d). Domains A1 and A2 are indistinguishable from each other in a neutron-scattering experiment because they have the same magnetic structure factor and domains B1 and B2 are also indistinguishable. However, an A-type (either A1 or A2) domain has a different structure factor from a B-type (either B1 or B2) domain.

2. Zero-field magnetic structure

The integrated intensity of magnetic Bragg peaks is related to the structure factor of the magnetic ordering through[19]

$$I(\mathbf{Q}) = \left(\frac{\gamma r_0}{2\mu_B}\right)^2 N_m \frac{(2\pi)^3}{V_{m0}} \Phi \frac{|f(\mathbf{Q})|^2}{\sin(2\Theta)} |F_\perp(\mathbf{Q})|^2, \quad (A6)$$

where $f(\mathbf{Q})$ is the magnetic form factor for Co^{2+} ions.[20] Φ is the flux of incident neutrons, N_m and V_{m0} are the number and the volume of the magnetic unit cells, $\gamma = 1.913$, and $r_0 = 2.818 \times 10^{-15}$ m. $I(\mathbf{Q})$ is the total integrated intensity of a Bragg reflection measured in the $(\Psi, 2\Theta)$ plane and $1/\sin(2\Theta)$ is the Lorentz correction factor that arises because intensity is measured as a function of angular coordinates. $\mathbf{F}_\perp(\mathbf{Q})$ is the component of the magnetic structure factor perpendicular to the scattering wave vector and is defined as

$$\mathbf{F}_\perp(\mathbf{Q}) = \mathbf{F}(\mathbf{Q}) - (\mathbf{F}(\mathbf{Q}) \cdot \hat{\mathbf{Q}})\hat{\mathbf{Q}}, \qquad (A7)$$

where $\hat{\mathbf{Q}}$ is the normalized wave-vector transfer.

The magnetic structure factor is defined as

$$\mathbf{F}(\mathbf{Q}) = \sum_{i=1}^{16} \mathbf{m}_i \exp(-i\mathbf{Q} \cdot \mathbf{d}_i), \qquad (A8)$$

where $\mathbf{Q}$ is the wave-vector transfer in the experiment, $\mathbf{d}_i$ are the positions of the Co^{2+} ions, and the sum is over all 16 magnetic ions in the magnetic unit cell. For a two-domain structure (A and B types) the magnetic Bragg-peak intensity can be written as

$$\mathbf{I}(\mathbf{Q}) = \alpha \mathbf{I}_A(\mathbf{Q}) + (1-\alpha)\mathbf{I}_B(\mathbf{Q}), \qquad (A9)$$

where α is the population of the A domain and $(1-\alpha)$ is the population of the B domain.

3. Absolute magnitude of the ordered moment

The magnitude of the ordered moment at $T = 80$ mK was determined by comparing the nuclear and the AF Bragg peak intensities. The intensity of a nuclear Bragg peak is given as

$$I(\mathbf{Q}) = N \frac{(2\pi)^3}{V_0} \Phi \frac{|F_N(\mathbf{Q})|^2}{\sin(2\Theta)}, \qquad (A10)$$

where N and V_0 are the number and the volume of the unit cells. $F_N(\mathbf{Q})$ is the nuclear structure factor and is given as[19]

$$F_N(\mathbf{Q}) = \sum_i b_i \exp(-i\mathbf{Q} \cdot \mathbf{d}_i), \qquad (A11)$$

where the sum runs over all elements in the nuclear unit cell and b_i is the elastic-scattering length[20] of atom i in the unit cell. The nuclear peaks used for calibration were $(02\bar{2})$, (033), (022), and $(03\bar{3})$ and their observed relative integrated intensities were consistent with the calculated structure factors to within 15%. Multiple-scattering and extinction corrections were assumed to be negligible. The measured nuclear intensities gave the overall scale factor for the intensities $A_{\exp} = N[(2\pi)^3/V_0]\Phi$ in Eq. (A10). The magnitude of the ordered magnetic moment was determined using $A_{\exp}$ and Eq. (A6). The resulting ordered moment at $T = 80$ mK in zero field is $m_0 = 1.7(4)\mu_B$.

[1] See, e.g., S. Sachdev, *Quantum Phase Transitions* (Cambridge University Press, Cambridge, England, 1999).

[2] D. Bitko, T. F. Rosenbaum, and G. Aeppli, Phys. Rev. Lett. **77**, 940 (1996).

[3] E. H. Lieb, T. Schultz, and D. J. Mattis, Ann. Phys. (N.Y.) **16**, 407 (1961).

[4] P. Jordan and E. Wigner, Z. Phys. **47**, 631 (1928).

[5] J. Kurmann, G. Müller, H. Thomas, M. W. Puga, and H. Beck, J. Appl. Phys. **52**, 1968 (1981).

[6] J. Kurmann, H. Thomas, and G. Müller, Physica A **112**, 235 (1982).

[7] H. Yoshizawa, G. Shirane, H. Shiba, and K. Hirakawa, Phys. Rev. B **28**, 3904 (1983).

[8] H. A. Algra, L. J. de Jongh, H. W. J. Blote, W. J. Huiskamp, and R. L. Carlin, Physica B & C **82B**, 239 (1976).

[9] S. Katsura, Phys. Rev. **127**, 1508 (1962).

[10] J. N. McElearney, S. Merchant, G. E. Shankle, and R. L. Carlin, J. Chem. Phys. **66**, 450 (1977).

[11] P. M. Duxbury, J. Oitmaa, M. N. Barber, A. van der Bilt, K. O. Joung, and R. L. Carlin, Phys. Rev. B **24**, 5149 (1981).

[12] In some of the earlier work (Refs. 10, 11, and 16) Cs_2CoCl_4 was associated with the space group *Pnam*, which is identical to *Pnma* but with the *b* and *c* axes interchanged.

[13] B. N. Figgis, P. A. Reynolds, and A. H. White, J. Chem. Soc. Dalton Trans. **7**, 1737 (1987).

[14] The definition of the atomic positions in the unit cell used here differs from the ones used in Figgis *et al.* (Ref. 13) by a shift of all positions by (0,0.5,0.5) in order to be consistent with R. W. G. Wyckoff, in *Crystal Structures* (Wiley, New York, 1965), Vol. 3, p. 100, and notation used by Algra *et al.* (Ref. 8).

[15] B. N. Figgis, M. Gerloch, and R. Mason, Proc. R. Soc. London, Ser. A **279**, 210 (1964).

[16] J. J. Smit and L. J. de Jongh, Physica B **97**, 224 (1979).

[17] G. Müller and R. E. Shrock, Phys. Rev. B **30**, 5254 (1984).

[18] V. Heine, in *Group Theory in Quantum Mechanics* (Dover, New York, 1993), pp. 119 and 288.

[19] G. L. Squires, *Thermal Neutron Scattering* (Cambridge University Press, Cambridge, England, 1978), Chap. 3, p. 42.

[20] A. J. C. Wilson, *International Tables For Crystallography* (Kluwer Academic, Dordrecht, 1995), Vol. C.